

meltPT: A Python package for basaltic whole-rock thermobarometric analysis with application to Hawai'i

• Fergus M^cNab*α and • Patrick W. Ball†β

- α Helmholtz Centre Potsdam, GFZ German Research Centre for Geosciences, Telegrafenberg, 14473 Potsdam, Germany.
- ^β Department of Geosciences, Colorado State University, Fort Collins, CO 80521, USA.

ABSTRACT

Quantifying the depths and temperatures from which igneous rocks are derived is an important step in understanding volcanic, magmatic and mantle processes. We present meltPT, a Python package that allows users to apply twelve published whole-rock thermobarometers within a consistent framework, as well as combine thermobarometric results and geothermal models to estimate mantle potential temperatures. We apply meltPT to basaltic rocks from mid-ocean ridges and the Hawaiian Islands. We find that mid-ocean ridge basalts equilibrate between 1–2 GPa and 1275–1475 °C, corresponding to an ambient mantle potential temperature of ~1400 °C. We estimate that the Hawaiian plume has an excess temperature of ~150 °C. Hawaiian melt-equilibration depths increase from 1–3 GPa to 2.5–5 GPa through each island's life cycle. Our results indicate that multiple lithologies are present within the plume, and that transient plume reconfiguration in response to changing plate velocity is a viable mechanism for generating Hawaii's two geochemically distinct plume tracks.

KEYWORDS: Thermobarometry; Geochemistry; Geodynamics; Python; Hawai'i; Mid-ocean Ridges.

1 Introduction

Volcanism is one of the clearest surface expressions of Earth's internal dynamics, but many open questions remain regarding melt generation and its links to mantle processes. Important unknowns are the depths and temperatures at which melting occurs, and how they vary as functions of time, space, and tectonic setting. Linking the compositions of volcanic rocks to the thermal state of the mantle from which they were derived is an important step in understanding why melting occurs where it does, and the diverse behaviour of volcanic centres around the world [McKenzie and O'Nions 1991; Kinzler and Grove 1992; Langmuir et al. 1992; Ito and Mahoney 2005; Putirka 2008a; Ball et al. 2021]. Quantifying depths and temperatures of mantle melting also provides rare observational constraints with which to test our understanding of the convecting mantle, its interactions with the overlying plate, and its evolution through deep time [e.g. Dalton et al. 2014; Condie et al. 2016; Klöcking et al. 2018; Brown Krein et al. 2021; Matthews et al. 2021; Ball et al. 2022].

In partially molten mantle, partitioning between melt and solid of major-element phases such as SiO_2 and MgO is sensitive to pressure and temperature. Many methods have been proposed that seek to calculate pressures and temperatures of melting from observed major-element compositions of volcanic rocks [e.g. Beattie 1993; Putirka et al. 2007; Putirka 2008b; Lee et al. 2009; Till et al. 2012; Grove et al. 2013; Herzberg and Asimow 2015; Plank and Forsyth 2016; Sun and Dasgupta 2020; Brown Krein et al. 2021]. There is often further interest in linking results of these analyses to mantle potential temperatures and/or lithospheric thicknesses, and various authors have proposed different methods for doing so [e.g. Plank

and Forsyth 2016; Reid et al. 2017; McNab et al. 2018; Brown Krein et al. 2021]. Whole-rock thermobarometers are commonly used tools in igneous petrology. For example, >2000 and >500 studies have referred to Putirka [2008b] and Lee et al. [2009], respectively. Despite this popularity, there currently exists no framework in which such methods can be applied and compared in a self-consistent and reproducible way.

One way to facilitate reproducible research is through the distribution of open-source software, an approach that is becoming increasingly prevalent in the geological community (see e.g. pymelt, for thermodynamic modelling of mantle melting [Matthews et al. 2022b]; thermobar, for meltcrystallisation thermobarometry [Wieser et al. 2022]). In this context, we present an open-source Python package for the performance of major-element thermobarometric analyses, which we call meltPT [McNab and Ball 2023]. Our package includes modules for estimating primary melt compositions, pressures and temperatures of melting, and for comparison of thermobarometric results with geothermal and meltproductivity models of the mantle. We provide a flexible environment that allows application of different combinations of analyses as desired, as well as straightforward integration of new thermobarometers, fractionation methods, and mantle melting parameterisations as they become available. Previous iterations of this software have been used successfully in studies of Borneo, Anatolia, North Africa, and Madagascar [e.g. M^cNab et al. 2018; Roberts et al. 2018; Ball et al. 2019; Stephenson et al. 2021. In the following, we briefly describe and discuss the basic methods and options available to users. We then present results from two case studies that highlight, in our view, the usefulness of this approach: the mid-ocean ridge system and the Hawaiian islands. meltPT is fully documented and the analyses presented here can be reproduced by following the tutorials provided (http://meltpt.readthedocs.io).

2 meltPT

Analyses in meltPT involve some combination of three steps. Major-element whole-rock thermobarometers are predicated on a chemical equilibrium between melt and solid maintained during mantle melting. However, melt compositions are expected to evolve as minerals begin to crystallise and are trapped during transport to the surface. Furthermore, volatile phases such as H2O and CO2 are often lost as the melt decompresses. Therefore, in a first step, we estimate original melt volatile contents and correct observed whole-rock majorelement compositions for the effects of fractional crystallisation in order to estimate their 'primary' compositions (i.e. their compositions when they were last in chemical equilibrium with the mantle). Then, in a second step, we calculate equilibration pressures and temperatures using the thermobarometeric schemes provided. Finally, we compare calculated equilibration pressures and temperatures with melting models to estimate associated melt fractions and mantle potential temperatures. In the following sections, we provide further details on each of these steps, illustrating the procedure using a sample from the Basin-and-Range Province, given by Plank and Forsyth [2016].

2.1 Estimating primary melt composition

2.1.1 Estimating volatile contents

Volatile phases such as H₂O and CO₂ play an important role in the partitioning of major elements during melting [Asimow and Langmuir 2003; Dasgupta et al. 2013]. As such, H₂O in particular is often included as a parameter in thermobarometric schemes [e.g. Lee et al. 2009; Herzberg and Asimow 2015; Plank and Forsyth 2016; Brown Krein et al. 2021]. Sun and Dasgupta [2020] also include CO₂ as a parameter in their scheme focused on deep melts. However, volatile phases can be easily lost as melts rise to the surface and decompress, and/or during sample preparation, so that whole-rock analyses are likely to underestimate their concentrations during melting. Thus, primary melt volatile concentrations must be estimated by other means. The state-of-the-art method is to measure their concentrations in melt inclusions trapped within olivine phenocrusts Plank and Forsuth 2016; Wieser et al. 2021]. Alternatively, a proxy can be used. For H₂O, the most commonly used proxy is Ce, which is thought to behave similarly to H₂O during melting, but be unaffected by degassing [e.g. Reid et al. 2017]. Thus, if the concentration of Ce is measured, and the ratio of H_2O to Ce in the source is known, melt H₂O can be estimated. The proportion of H₂O with respect to Ce in the mantle can vary between 0 and 1000 depending on geologic history and present-day setting Ruscitto et al. 2012. In meltPT, individual sample H₂O concentrations can be specified if they are independently known, calculated from Ce concentrations with a chosen value of source H₂O/Ce, or treated as anhydrous. Similarly, we include the scheme of Sun and Dasgupta [2020], in which CO₂ concentrations are parameterised in terms of SiO₂ contents, for use in their thermobarometric scheme, designed for deep, CO₂-rich, SiO₂-poor melts.

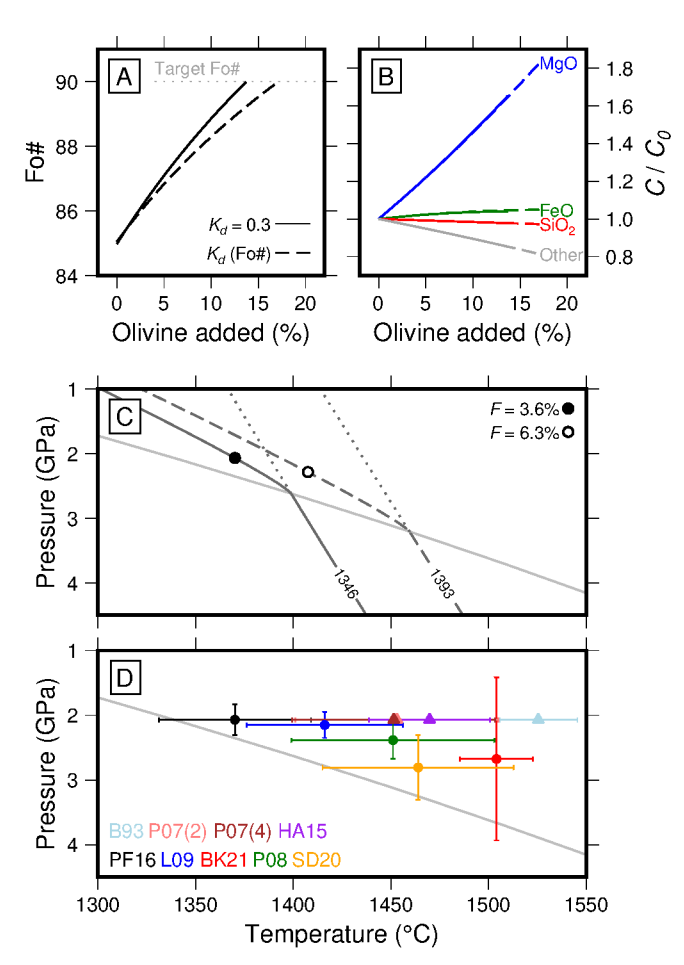


Figure 1: Worked example for Sample UT09DV04 Plank and Forsyth 2016]. [A] Fo# of olivine in equilibrium with the melt as a function of olivine addition to Fo# = 90. Solid/dashed lines = correction pathways assuming a constant/variable olivinemelt partition coefficient (K_d) . [B] Major-element oxide concentrations, C, normalised by their initial concentrations, C_0 , as a function of olivine addition. Solid/dashed lines = constant/variable K_d . [C] Filled/open circles = thermobarometric estimate assuming constant/variable K_d [Plank and Forsyth 2016]. Gray line = anhydrous solidus; solid/dashed lines = best-fitting melting pathways for constant/variable K_d cases, labelled with corresponding T_p ; dotted lines = adiabatic decompression pathways corresponding to melting pathways [Katz et al. 2003]. [D] Results from different schemes currently implemented in meltPT. Backtracking carried out assuming $K_d = 0.3$. Circles = thermobarometric results; triangles = thermometric results, assuming pressure from Plank and Forsyth [2016]. Colour-coded according to scheme, as shown in bottom left. PF16 = Plank and Forsyth [2016]; L09 = Lee et al. [2009]; BK21 = Brown Krein et al. [2021]; P08 = Putirka [2008a]; SD20 = Sun and Dasgupta [2020]; B93 = Beattie [1993]; P07(2) and P07(4) = Putirka et al. [2007], Equations (2) and (4), respectively; HA15 = Herzberg and Asimow [2015].

2.1.2 Correcting for fractionation

In typical mantle melts the first phase to begin crystallising is olivine, the clearest effect of which is to reduce the Mg content of the melt. Subsequent crystallisation of phases such as plagioclase and clinopyroxene leads to a more complicated compositional evolution. Some previous workers have therefore invoked a threshold MgO content, for example around 8.5 wt%, below which samples are rejected, and corrected only for crystallisation of olivine [Lee et al. 2009; Plank and Forsyth 2016, while others have performed more complex corrections for other crystallising phases [e.g. Till et al. 2012; Brown Krein et al. 2021]. In meltPT, to limit the number of free parameters introduced by additional corrections, we have implemented the former approach. Users also have the option of determining primary melt compositions by external methods and then applying meltPT's thermobarometric capabilities. We also note that meltPT is designed in a modular way to allow the straightforward encorportation of alternative fractionation corrections in the future, such as those of Till et al. [2012] and Brown Krein et al. [2021].

We correct for the effects of olivine fractionation using a procedure described by Lee et al. [2009]. First, we calculate the forsterite number, Fo#, of olivine in equilibrium with a given melt using the formula

Fo# =
$$\left(1 + K_d \frac{\text{Fe}^{2+}}{\text{Mg}}\right)^{-1} \times 100 = \frac{\text{Mg}_{\text{ol}}}{\text{Mg}_{\text{ol}} + \text{Fe}_{\text{ol}}^{2+}} \times 100, \quad (1)$$

where Mg and Fe²⁺ are the cation concentrations of the melt in mol% and subscript "ol" indicates the cation concentration in olivine. The partition coefficient, K_d , between olivine and melt can be set to a constant value (e.g. ~0.3) or calculated as a function of melt Fo# [after Tamura et al. 2000]. We then add a small amount of olivine with this composition (e.g. 0.1 wt%) to the melt. We repeat this process iteratively until the melt composition reaches a Fo# thought to correspond to the onset of olivine crystallisation. The Fo# of mantle-derived olivine xenocrysts in kimberlites and basalts typically range from 86–91. An appropriate value for a given region can be estimated using the compositions of olivine phenocrysts, xenocrysts or xenoliths [e.g. Section 4.1; Plank and Forsyth 2016].

In our example, the sample begins with Fo# ~85 (Figure 1A). Plank and Forsyth [2016] estimated the Fo# to be ~90 in the source region of the Basin-and-Range Province. If K_d is fixed to 0.3, as in Plank and Forsyth [2016], the sample composition reaches the target value of Fo# = 90 after the addition of approximately 14 % olivine. If K_d is allowed to vary as a function of Fo#, slightly more olivine addition is required (~17 %). In this example, olivine addition increases sample MgO content by ~1.8 times, FeO and SiO₂ concentrations remain approximately constant, while remaining major-element oxides, which are incompatible in olivine, are slightly diluted (Figure 1B).

A final important variable must be constrained before this procedure can be applied: the proportion of ferrous to ferric iron in the melt. Only ferrous iron, Fe^{2+} , is exchanged with olivine; any ferric iron, Fe^{3+} , is retained in the melt. However, their relative proportion, generally expressed as the ratio of ferrous to total iron contents, $Fe^{2+}/\Sigma Fe$, depends on the melt's oxidation state, which can evolve during transport to the surface. Thus, measured $Fe^{2+}/\Sigma Fe$ for a given sample

may not reflect $Fe^{2+}/\Sigma Fe$ of the melt during olivine crystallisation. As with melt volatile contents, $Fe^{2+}/\Sigma Fe$ would ideally be estimated for individual samples or on a regional basis by analysing melt inclusions trapped during crystallisation. Alternatively, vanadium can be used as a proxy for melt oxygen fugacity, from which melt $Fe^{2+}/\Sigma Fe$ can be predicted [Kress and Carmichael 1991; Canil 2002; Plank and Forsyth 2016]. Primary melt $Fe^{2+}/\Sigma Fe$ values tend to vary between ~0.1–0.4 [Brounce et al. 2014].

2.2 Whole-rock thermobarometry

Once primary melt compositions have been estimated, thermobarometric schemes can be applied. In the current version of meltPT, we have implemented twelve such schemes (Table 1). They generally take similar forms and are derived in similar ways. Experimental measurements of melt-solid equilibrium compositions, using either natural or synthetic mantle rocks, are made or compiled for a range of pressuretemperature conditions, compositions, and lithologies. These databases can then be used to calibrate parameterisations of pressure and temperature as functions of melt composition. Studies differ in their choices of experimental data and phases with which to construct their parameterisations. The thermobarometers implemented in meltPT therefore differ in the pressure, temperature, and compositional ranges over which they are valid. We urge users to familiarise themselves with the assumptions and limitations of any specific thermobarometers they choose to apply with meltPT.

Continuing with our worked example, for the $K_d=0.3$ case we obtain P=2.07 GPa and T=1370 °C from the sample's primary composition (Figure 1D), in close agreement with the result of Plank and Forsyth [2016, their Supplementary Table S8]. For the variable K_d case we obtain P=2.29 GPa and T=1407 °C. In Figure 1D, we show results of applying to this sample a selection of other thermobatometers currently implemented in meltPT.

2.3 Estimating melt fractions and T_p

To compare equilibration pressures and temperatures across geologic settings, and begin to understand their differences and similarities, it is useful to compare them with physical models of the mantle geotherm and/or melting processes. In meltPT, we implement a revised version of the method used in M^cNab et al. [2018]. This approach estimates mantle potential temperature, T_p , and melt fraction, F, by fitting pressure-temperature-melt fraction paths to individual, or suites of, equilibrium pressure-temperature estimates. To compute melting paths we use the pyMelt package, which incorporates several published models and allows hydrous mantle consisting of multiple lithologies to be considered [Matthews et al. 2022a; b]. We find best-fitting melting paths for a given sample, or suite of samples, using a two-step procedure. First, we find the closest pressure-temperature point on a given melting path for a given sample by minimising the euclidean distance, D, between the melt path (P_m, T_m) and

Table 1: List of thermobarometric schemes currently offered by meltPT. Equations refer to equation numbers in the listed publications. All thermobarometers can be used as thermometers and barometers but some require *P* or *T* as an input parameter, respectively. For up-to-date lists of thermobarometric schemes currently implemented in meltPT, visit our online documentation: https://meltpt.readthedocs.io.

Publication	<i>T</i> (°C)	P (GPa)
Thermobarometers		
Putirka [2008b], Equations 22, 42	965-2080	0.0 - 15.5
Lee et al. [2009]	1100-1800	0.0 - 7.0
Till et al. [2012]	1090-1590	0.9 - 3.4
Plank and Forsyth [2016]	1250-1870	0.0 - 3.0
Sun and Dasgupta [2020]	900-1968	1.6 - 10.0
Brown Krein et al. [2021]	1250-1755	1.0 - 6.0
Thermometers		
Beattie [1993]	1060-1860	0.0 - 4.0
Putirka et al. [2007], Equation 2	1000-2000	0.0 - 15.5
Putirka et al. [2007], Equation 4	1000-2000	0.0 - 15.5
Herzberg and Asimow [2015]	1025-2020	0.0 - 14.0

sample (P_s, T_s) pressure and temperature:

$$D = \sqrt{\left(\frac{P_s - P_m}{\sigma_P}\right)^2 + \left(\frac{T_s - T_m}{\sigma_T}\right)^2},\tag{2}$$

where pressure and temperature differences are normalised by their respective uncertainties, σ_P and σ_T . Note that best-fitting P_m and T_m also correspond to an estimate of melt fraction for the sample. We then search for the T_p that minimises either D for an individual sample or the mean D of a suite of samples. Any samples that are below the solidus by $> \sigma_T$ are ignored during this procedure since they do not lie along a calculated melt path. For our worked example, using the (anhydrous) lherzolite melting model of Katz et al. [2003], we find a best-fitting potential temperature of 1346 °C and corresponding melt fraction of 3.6 % for the $K_d=0.3$ case, and 1392 °C and 6.3 % for the variable K_d case (Figure 1C).

2.4 Uncertainties

Each of the processing steps described above introduces uncertainty into estimates of equilibration pressure, equilibration temperature, and hence mantle potential temperature. The thermobarometric parameterisations themselves are regressions to experimental data, and a measure of uncertainty based on the goodness of fit is generally provided (such as those shown in Figure 1D). Where available, these uncertainties are integrated into meltPT and included whenever pressure and temperature estimates are output.

Uncertainties are also introduced during estimation of primary sample compositions. A lack of independent evidence concerning the actual primary compositions of mantle melts and the effects of fractional crystallisation means that the accuracy of these methods is difficult to assess. We can, however, assess the impacts of uncertainties in the various input

parameters. If meaningful bounds can be placed on the values of these parameters, these uncertainties can be propagated through to uncertainties in pressure, temperature and mantle potential temperature using a Monte Carlo approach. Such analysis is straightforward to implement using meltPT (see Texts S1 and S2 and Figures S1–S5 in Supplementary Material 1 for examples).

Finally, when estimating mantle potential temperature using a suite of samples, uncertainty arises due to the dispersion of the estimated equilibration pressures and temperatures. We attempt to quantify this dispersion by first dividing the set of samples in two, treating those that lie warmer or cooler than the best-fitting melting path separately. We then define an upper-bound melting path such that two thirds of the 'warmer' samples lie between it and the best-fitting melt path. Similarly, two thirds of the 'cooler' samples lie between our lower-bound and best-fitting melting paths. As such, these bounds correspond approximately to one-standard-deviation uncertainties for our T_p estimates.

2.5 Implementation

meltPT and pyMelt offer a wide range of thermobarometric schemes and possible melting conditions, respectively. Rather than exploring differences between these options, in Sections 3 and 4 we showcase the power of meltPT to tackle geologic problems. Therefore, we exploit a single method: the thermobarometric scheme of Plank and Forsyth [2016] coupled with an anhydrous lherzolitic mantle source [Katz et al. 2003]. To limit errors from the crystallisation of non-olivine phases, we only accept samples with MgO > 8.5 wt%. The Plank and Forsyth [2016] thermobarometer assumes the coexistence of olivine and pyroxene. To ensure this assumption is applicable, we only accept primary melts with $SiO_2 > 40$ wt%. We perform the fractional crystallisation correction with a variable K_d . We estimate values of H_2O/Ce , source Fo#, and melt Fe³+/ Σ Fe on the basis of local constraints, which we discuss further below.

3 ESTIMATING AMBIENT MANTLE T_P

It is often useful to provide context for thermobarometric results by comparing them to a reference ambient-mantle T_p . Systematic differences in T_p estimates obtained by different methods imply that different reference values should be used depending on which thermobarometric and melt productivity schemes are chosen [e.g. Ball et al. 2021]. Mid-ocean ridges (MORs) are widely distributed across Earth's surface and their locations are determined by plate motions rather than mantle temperature variations [Forsyth and Uyeda 1975]. We therefore assume that MORs sample a wide range of upper mantle temperatures that can be combined to estimate an average ambient value. Here, we apply our thermobarometric approach to the mid-ocean ridge basalt (MORB) database of Gale et al. [2013], with a view to estimating ambient mantle T_p for our chosen meltPT set-up.

Thermobarometric calculations are conducted on this MORB database assuming that Fo#, Fe $^{+3}/\Sigma$ Fe, and H₂O/Ce are 90, 0.14, and 200, respectively [Lee et al. 2009; Zhang et al. 2018; Yang et al. 2021]. We only permit MORB sam-

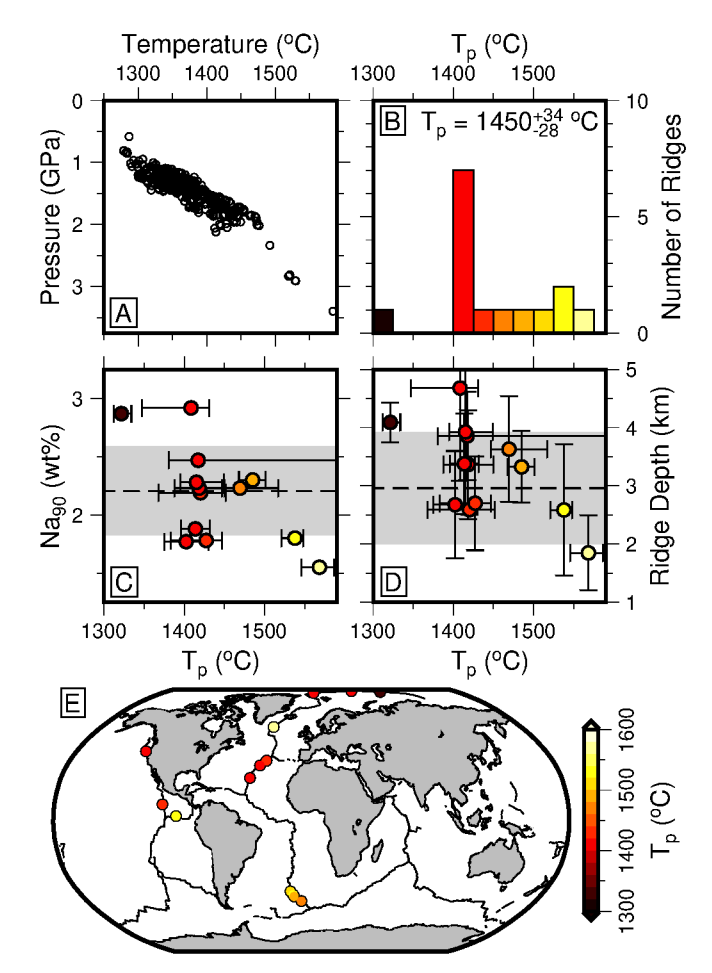


Figure 2: Thermobarometric T_p estimates for mid-ocean ridges (MOR). [A] Melt equilibration estimates for all viable MOR samples [Gale et al. 2013]. [B] Histogram of MOR T_p estimates for ridge segments with >5 melt equilibration estimates. Average T_p and errors shown top left. [C] MOR T_p estimates as a function of ridge Na $_{90}$ values; dashed line and gray swath show average and standard deviation of global MOR Na $_{90}$ database [Gale et al. 2014]. [D] Same as Panel [C] for ridge-depth measurements [Gale et al. 2014]. [E] World map with colored circles indicating locations and best-fitting T_p estimates of MORs with >5 thermobarometric results.

ples with recorded Ce values to ensure that H_2O concentrations can be estimated. Our results show that the vast majority of MORBs equilibrated at pressures and temperatures between 1–2 GPa and 1275–1475 °C, respectively (Figure 2A). We only use ridge segments to estimate T_p that have ≥ 5 melt-equilibration results, resulting in 15 locations worldwide. Our best-fitting ridge-segment T_p estimates range between 1321–1568 °C, with an average temperature of 1450 °C (Figure 2B). Our T_p estimates negatively correlate with Na₉₀ and bathymetric-depth observations which are commonly expected to be inversely proportional to mantle temperature [Figure 2C and D; Dalton et al. 2014].

The global coverage of our ridge-segment T_p estimates is somewhat limited since only ~15 % of MORB samples have MgO contents ≥ 8.5 wt% [Figure 2E; Gale et al. 2013]. Ap-

proximately half of our ridge segments have best-fitting T_p between 1400–1425 °C, and ridges with best-fitting $T_p > 1450$ °C overlie the Iceland, Bouvet, Galápagos, and Meteor mantle plumes. Melts generated at plume-adjacent ridges are therefore probably over-sampled in our database; we discount them when estimating ambient mantle T_p . Using ridge segments with best-fitting T_p of < 1450 °C, we calculate an ambient mantle T_p of ~1402 °C.

4 Application to Hawai'i

The Hawaiian islands are one of the most well-characterised volcanic regions on Earth, providing an ideal test case for our thermobarometric approach. The subaerial Hawaiian Islands

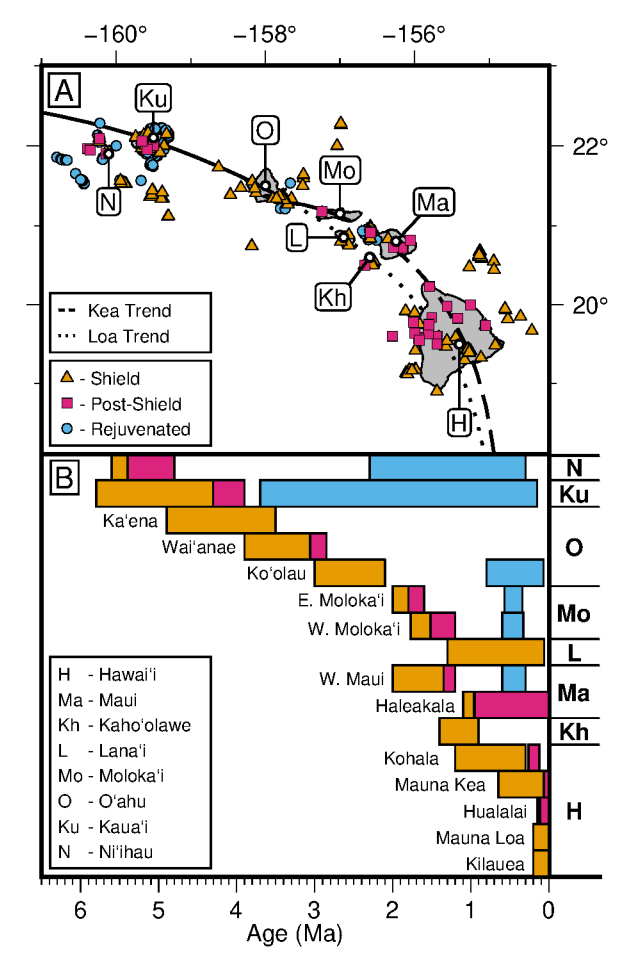


Figure 3: Location and stratigraphy of the Hawaiian islands. [A] Map with Hawaiian islands in gray, letters indicate island names as described in lower left of figure. Orange/pink/blue symbols = basaltic samples from shield/post-shield/rejuvenated phases of volcanism used for thermobarometric analysis. Solid/dashed/dotted lines = combined/Kea/Loa volcanic tracks [taken from Jones et al. 2017]. [B] Stratigraphic lexicon of Hawaiian islands and their volcanoes [as denoted by letters along the right-hand side and names listed on the left-hand side, respectively; Clague and Frey 1982; Cousens and Clague 2015; Sinton et al. 2017]. Bar color = phase of volcanism.

lie at the eastern tip of the Hawaiian and Emperor seamount chains, which were generated by the Pacific plate translating over the Hawaiian mantle plume since ~80 Ma [Clague and Dalrymple 1987]. The islands are aligned northwest-southeast and exhibit age-progressive volcanic activity (Figure 3A). The oldest eruptions on the most northwesterly and most southeasterly islands of Kaua'i and Hawai'i are dated to ~5.8 Ma and ~1.2 Ma, respectively [Figure 3B; Cousens and Clague 2015; Sinton et al. 2017].

The life cycle of a Hawaiian volcano is commonly subdivided into four distinct phases. First, low-volume alkaline lavas erupt in a pre-shield phase [Clague and Dalrymple 1987]. Second, huge volumes of theoliitic basalts are generated and form a shield volcano. Third, the shield is capped by a post-shield evolved alkaline phase. Finally, after a repose of between ~0.6–2 Ma, a series of highly alkaline, low-volume, rejuvented-phase eruptions can occur [Clague and Sherrod 2014]. All four phases are not necessarily present at each volcano and they vary greatly in spatial and temporal extent (Figure 3B). Due to limited data coverage for the pre-shield phase, we focus on the final three phases here.

Approximately 3 Ma, two spatially separated and geochemically distinct volcanic trends appeared along the Hawaiian island chain [Figure 3A; Frey and Rhodes 1993]. Volcanic products from Moloka'i, Maui, and the northeastern side of Hawai'i (the 'Kea' trend) are less isotopically enriched and exhibit higher CaO/SiO₂ and Ti/Na ratios than their equivalents from Lāna'i, Kaho'olawe, and the southwestern volcanoes of Hawai'i [the 'Loa' trend; Frey and Rhodes 1993; Abouchami et al. 2005].

Despite the wealth of data and work characterising Hawaiian volcanism, a series of important unknowns remain. These include: the excess temperature of the underlying mantle plume, and the causal mechanisms that generate the rejuvenated phase and the Mauna/Kea geochemical trends. Here, we apply our thermobarometric approach to each island in turn and attempt to address these outstanding issues.

4.1 Data collection and model set-up

To explore pressures and temperatures of melting beneath Hawai'i, we use an updated and revised version of the global database of Ball et al. [2021], assigning each sample to an eruptive phase according to the original authors' definition (note that precise definitions differ between studies; Figure 3A; Supplementary Material 2). Most samples in our database cannot be linked directly to measurements of melt H_2O content, source Fo#, or melt $Fe^{+3}/\Sigma Fe$. Before performing thermobarometric analyses, we therefore need to estimate these values for the Hawaiian islands.

 H_2O and Ce concentrations of olivine-hosted melt inclusions and volcanic glasses for samples from across the Hawaiian Islands are detailed in Supplementary Material 3 and Table 2. Average H_2O/Ce values and their standard deviations for the shield, post-shield and rejuvenated phases are $144\pm 56, 136\pm 62$ and $211\pm 29,$ respectively. Within this database, we observe strong positive correlations between H_2O/Ce and H_2O values in shield and post-shield data (Figure 4A). Assuming that H_2O and Ce have the same bulk partition coefficient,

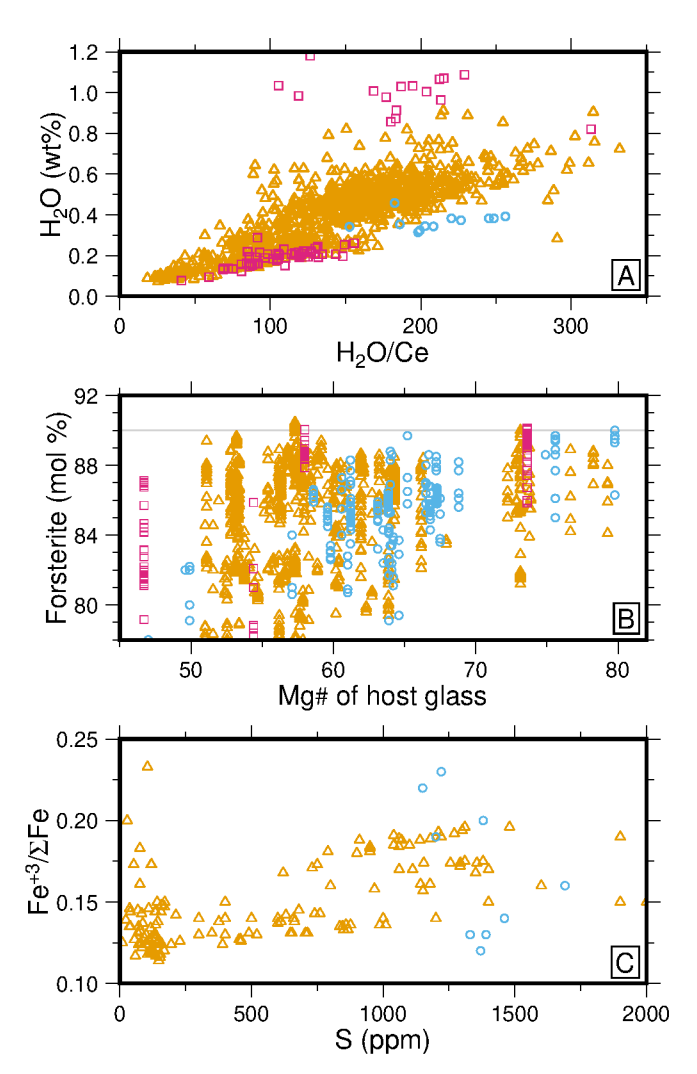


Figure 4: Hawaiian islands geochemical data (see Table 2 for details). [A] H_2O content of melt as a function of H_2O/Ce . Colored triangles/squares/circles denote geochemical data from shield/post-shield/rejuvenated volcanic phases. [B] Rhodes diagram showing Fo# of olivines as a function of whole-rock Mg#. Gray line shows Fo# = 90 for reference. [C] $Fe^{+3}/\Sigma Fe$ of melt as a function of S content.

these correlations indicate that H_2O concentrations are either highly variable within the mantle source, or significantly affected by hydrogen diffusion. If the former is true, we can use the average value for each phase and acknowledge that this value is highly uncertain. However, if the latter is true our H_2O/Ce values are underestimates and the true value may be ≥ 300 (Figure 4A; the implications of varying each parameter within acceptable limits is discussed in Section 4.3.2).

To estimate Fo# of the primary melt, we compiled a database of Hawaiian olivine compositions (Supplementary Material 3). This database includes olivines from all three eruptive phases and from a range of islands (Table 2). We assume that the most forsteritic olivine phenocrysts observed were among the first to crystallise and reflect primary melt compositions. From all three phases, the most forsteritic olivines have Fo# \approx 90; we use this value for the primary

Table 2: Model parameters for calculating melt-equilibration conditions for the Hawaiian Islands. H_2O , Ce, Fo#, and Mg# data from melt inclusions and their olivine hosts shown in Database S2; $Fe^{+3}/\Sigma Fe$, S, and Mg# data shown in Database S3. Volcanoes: Hk = Haleakala; Hl = Haulalai; Ka = Kauai; Kk = Koko; Kl = Kīlauea; Ko = Koolau; Ku = Kaula; L = Lōi'hi; ML = Mauna Loa; N = Ni'ihau; NA = North Arch. References: 1 = Brounce et al. [2017]; 2 = Dixon et al. [1997]; 3 = Dixon and Clague [2001]; 4 = Dixon et al. [2008]; 5 = Garcia et al. [2015]; 6 = Garcia et al. [2016]; 7 = Garcia et al. [2022]; 8 = Helz et al. [2017]; 9 = Marske and Hauri [2019]/Tucker et al. [2019]; 10 = Moore et al. [2021]; 11 = Moussallam et al. [2016]; 12 = Sakyi et al. [2012]; 13 = Sides et al. [2014]; 14 = Wieser et al. [2019].

Phase	H ₂ O/Ce	Volcanoes	Refs.	Fo#	Volcanoes	Refs.	Fe ⁺³ /ΣFe	Volcanoes	Refs.
Shield	144	Kl,L,ML	3,9,13	90	Ka,Kl,Ko,L,ML	5,9,12,13,14	0.15	Kl,ML	1,8,11
Post-Shield	136	Hk,Hl,Ko	9,10	90	Hk,Hl,Ko	9,10	0.15	no data	no data
Rejuvenated	211	N	4	90	Ka,Kk,Ko,Ku	5,6,7,12	0.17	NA	2

melt in our thermobarometric calculations (Figure 4B). Some studies of Hawaiian eruptions report that the most forsteritic olivines are not co-genetic with their host lavas [e.g. Wieser et al. 2019]. If these 'alien' olivines crystallised out of another melt with the same source before mixing into the final lava, our chosen mantle Fo# remains valid. However, if these olivines are mantle xenocrysts then our Fo# could be overestimates. Nearly all studied eruptions include olivines with Fo# \approx 89, which we treat as a lower bound.

Database S3 (Supplementary Material 4) also includes a suite of $\mbox{Fe}^{+3}/\Sigma\mbox{Fe}$ analyses of melt inclusions and volcanic glasses from the Hawaiian Islands (see Table 2 for details). Melt $Fe^{+3}/\Sigma Fe$ values change as volatile phases and/or ferrous minerals exsolve [Sato 1978]. These processes appear to affect melt oxidation data from Hawai'i, evidenced by a correlation between S and Fe⁺³/ Σ Fe [Figure 4C; Moussallam et al. 2016; Brounce et al. 2017; Helz et al. 2017]. Our aim here is to parameterise the predominant Fe⁺³/ Σ Fe ratio present during fractional crystallisation; we therefore average all available data. If degassing occurred prior to the onset of crystallisation, average $Fe^{+3}/\Sigma Fe$ values will represent average crystallisation conditions. However, if degassing began towards the end of crystallisation, average $Fe^{+3}/\Sigma Fe$ ratios will be underestimates and the true value may be as high as 0.2 (Figure 4C). Average $Fe^{+3}/\Sigma Fe$ values for the shield- and rejuvenated-phase are 0.15 ± 0.02 and 0.17 ± 0.04 , respectively. To our knowledge, there are no $Fe^{+3}/\Sigma Fe$ data published for post-shield phase samples and so we assume the same $Fe^{+3}/\Sigma Fe$ ratio for the shield and post-shield phases.

4.2 Results

We present Hawaiian melt-equilibration pressures and temperatures subdivided by island (Figure 5A–F). Note we combine data from the geographically proximal Ka'ula and Ni'ihau, from Moloka'i and Maui, and from Kaho'olawe and Lāna'i, since there are fewer data available from each and their geochemical characteristics are similar. In each case, results span ranges of pressures and temperatures that are consistent with paths of adiabatic decompression melting. Our results suggest that shield-, post-shield- and rejuvenated-phase melts are generated via adiabatic upwelling at similar potential temperatures but that their melts last equilibrated at different pressures (~1–3 GPa, ~1.5–3.5 GPa and ~3–5 GPa, respectively).

Major-element pressure distributions can be corroborated using trace-element data [e.g. Ball et al. 2019]. Lighter rareearth elements, such as Sm, are less compatible in garnet than heavier rare-earth elements, such as Yb [Shimizu and Kushiro 1975]. Since garnet is only present in the mantle at pressures $\gtrsim 2$ GPa, high Sm/Yb ratios in melts are indicative of deep melting [i.e. > 2 GPa; Kay and Gast 1973]. Positive correlations between melt-equilibration pressures and Sm/Yb corroborate the distribution of pressures we obtain by thermobarometric methods (Figure 5G–L). This correlation also implies that melt-equilibration pressure/temperature estimates do indeed represent different points along a consistent melting path and suggests that melts generated within the asthenosphere can ascend through > 100 km of mantle and crust without reequilibrating.

Our melt-equilibration results can be combined or divided in a number of different ways to estimate T_p of the Hawaiian mantle plume (Table 3). When all available data are taken together, we estimate that the mantle beneath the Hawaiian Islands has a T_p of 1555 °C, equivalent to an excess temperature of ~150 °C (Figure S6A; see Supplementary Material 1). We note that the Plank and Forsyth [2016] thermobarometer was calibrated using samples that equilibrated at pressures less than 3 GPa; our T_p estimate does not change significantly when samples estimated to equilibrate at > 3 GPa are excised (Table 3; Figure S6B). If we divide our melt-equilibration data by volcanic phase, we obtain similar T_p for shield and post-shield phases (1556 $^{+20}_{-25}$ °C and 1556 $^{+42}_{-29}$ °C, respectively; Figure S4D, E). In contrast, we calculate a colder and less well-constrained T_p for the rejuvenated phase (1517 $^{+95}_{-60}$ °C; Figure S6F).

We also subdivide our melt-equilibration estimates according to island grouping (Figure 5A–F). With the exception of Ni'ihau and Ka'ula, best-fitting T_p estimates for all Hawaiian islands are within error of each other (~1530–1560 °C). Small variations in T_p between islands broadly reflect the proportion of rejuvenated phase data present (i.e. colder temperatures are predicted for older islands with more rejuvenated-phase data).

4.3 Discussion

4.3.1 Comparison with previous work

Several previous studies have estimated T_p for the Hawaiian mantle plume, with a wide range of results. Recent calibrated

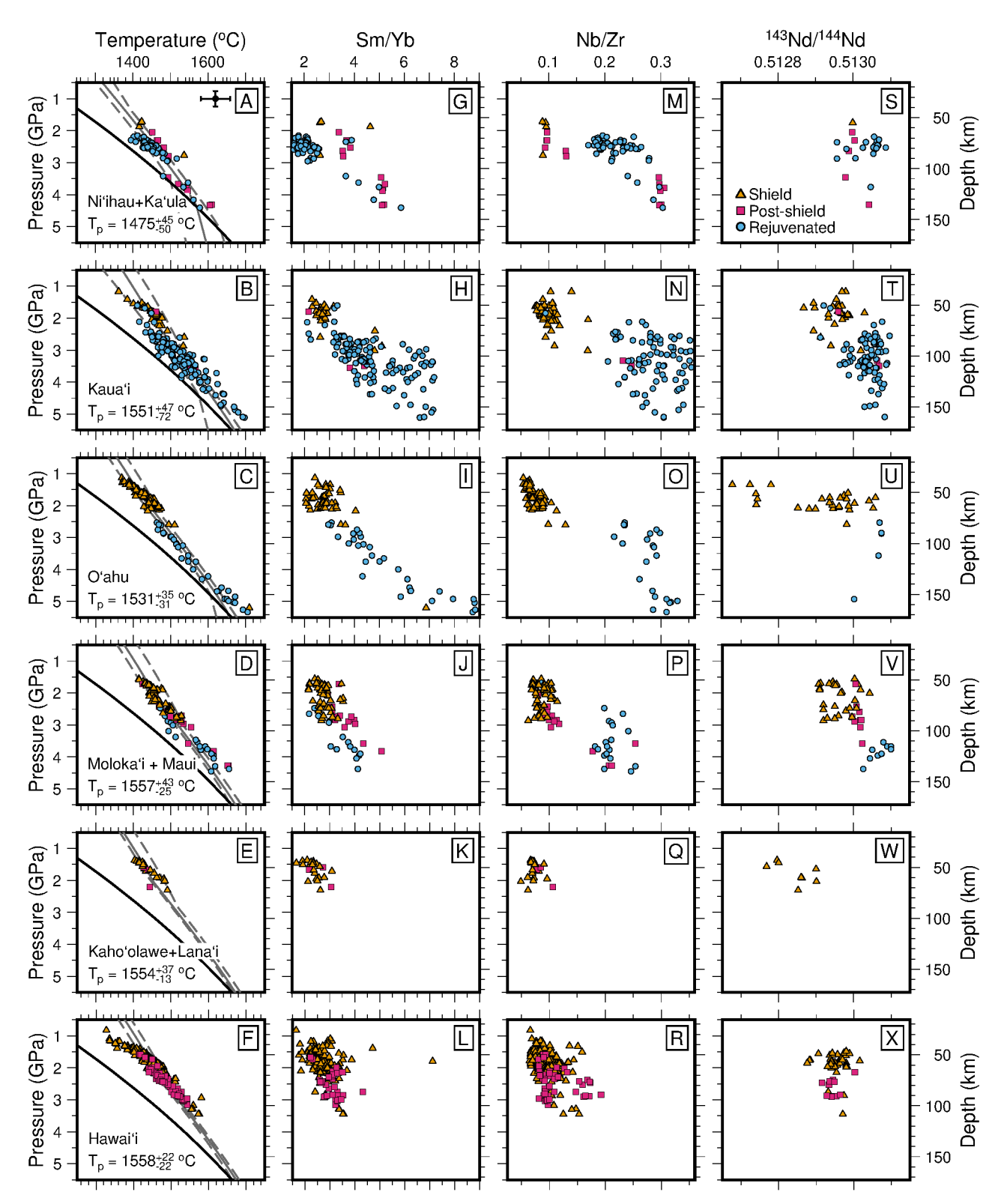


Figure 5: [A] Temperature plotted as function of depth/pressure. Symbols = equilibration pressure/temperature estimates determined for mafic samples from Ni'ihau and Ka'ula using formulation of Plank and Forsyth [2016] and parameters in Table 2. Orange/pink/blue symbols = shield/post-shield/rejuvenated phase data. Black line = anhydrous solidus; gray line = best-fitting melt pathway; dashed gray lines = minimum and maximum melt pathways for which misfit value at global minimum is double [Katz et al. 2003]; optimal value of T_p = 1475 $^{+45}_{-50}$ °C. Black point with error bars in top right displays the errors associated with this thermobarometric method [39 °C, 0.24 GPa; Plank and Forsyth 2016]. [B] Kaua'i. [C] O'ahu. [D] Moloka'i and Maui. [E] Kaho'olawe and Lāna'i. [F] Hawai'i. [G]–[L] Same as Panels [A]–[F] but with Sm/Yb ratios plotted as function of calculated pressures. [S]–[X] Same as Panels [A]–[F] but with 143 Nd/ 144 Nd ratios plotted as function of calculated pressures.

Table 3: Estimated potential and excess temperatures (T_p and T_{ex} , respectively) for Hawaiian Islands. Extrema calculates thermobarometric conditions using H₂O/Ce = 300, Fo# = 89, and Fe⁺³/ Σ Fe = 0.2.

		T_p (°C)	T_{ex} (°C)	Figure
All	Data	1555^{+28}_{-51}	153	S6A
All	Data (< 3 GPa)	1555^{+24}_{-43}	153	S6B
All	Data (Extrema)	1414^{+36}_{-44}	12	S6C
	Shield	1556 ⁺²⁰ ₋₂₅	154	S6D
Phase	Post-shield	1556^{+42}_{-29}	154	S6E
Д	Rejuvenated	1517^{+95}_{-60}	115	S6F
	Niʻihau & Kaʻula	1475 ⁺⁴⁵ ₋₅₀	63	5A
	Kaua'i	1551^{+47}_{-72}	149	5 B
pu	Oahu	1531^{+35}_{-31}	129	5C
Island	Molokaʻi & Maui	1557^{+43}_{-25}	155	5D
	Kahoʻolawe & Lanaʻi	1554^{+37}_{-13}	152	5 E
	Hawai'i	1558^{+22}_{-22}	156	5F
pu	Loa	1544 ⁺²⁹	142	6A
Trend	Kea	1560^{+24}_{-21}	158	6C

seismic tomographic studies calculate T_p of 1402 °C [Hoggard et al. 2020] and 1559 °C [Bao et al. 2022] which equate to excess potential temperatures (T_{ex}) of 69 °C and 171 °C, respectively. T_p estimates using liquid-olivine distribution of MgO range from 1499 \pm 17 °C to 1630 \pm 77 °C [Courtier et al. 2007; Putirka et al. 2018, respectively]. Potential temperatures calculated using spinel-olivine Al-exchange thermometry vary between 1402 $^{+69}_{-45}$ °C and 1582 $^{+68}_{-65}$ °C [Matthews et al. 2021]. Finally, T_p estimates of 1526 °C and 1361 °C (T_{ex} = 46 °C) have been obtained using major- and trace-element whole-rock compositions (Herzberg and Asimow [2015] and Ball et al. [2021], respectively). Our T_p estimate of ~1530–1560 °C (T_{ex} = 125–155 °C) therefore lies within the range of existing estimates for the Hawaiian mantle plume.

4.3.2 Uncertainties in mantle conditions

Assumed mantle composition and crystallisation conditions can have a significant impact on melt-equilibration results. Our chosen $\rm H_2O/Ce$, Fo#, and Fe $^{+3}/\Sigma$ Fe values are minimum, maximum, and minimum estimates, respectively. Therefore, our T_p predictions can be considered upper bounds. Changing these parameters to their respective extrema lowers T_p by ~140 °C (Table 3; Figure S6C). However, assuming that these parameters do not vary significantly between islands, comparisons between the Hawaiian islands and their volcanic phases will not be affected by uncertainties in the precise values chosen. Moreover, plausible discrepancies in these parameters cannot account for the significant variations in meltequilibration pressures we observe, which are consistent with distributions of Sm/Yb (Figure 5G–L). We therefore argue

that observed increases in melt-equilibration pressures (and, hence, decreases in melt fractions) over the eruptive-phase cycle are robust features of our analysis. We further illustrate possible consequences of uncertainties in these parameters using a Monte Carlo analysis in Supplementary Material 1 (Text S2; Figures S2–S5).

4.3.3 Generating the rejuvenated phase

The rejuvenated phase begins ~0.6–2 Ma after the post-shield phase ends and has been an established part of the Hawaiian volcanic cycle since at least 12.5 Ma [Harrison et al. 2020]. Rejuvenated-phase lavas have consistently higher Nb/Zr and ¹⁴³Nd/¹⁴⁴Nd ratios than shield or post-shield lavas, an observation that has been used by multiple authors to suggest that the source for rejuvenated-phase samples is compositionally distinct from the other phases [Figure 5M–X; e.g. Ballmer et al. 2011; Hofmann and Farnetani 2013; Garcia et al. 2016; Borisova and Tilhac 2021]. Mechanisms that attempt to explain the generation of the rejuvenated phase should therefore account for an eruptive hiatus and a change in source composition.

There are three plausible ways to modify source composition during an island's eruptive cycle. First, metasomatised lithospheric mantle could be remobilised as lithospheric material is heated, from below by the plume and/or from within by rising melts [Chen and Frey 1985; Gurriet 1987]. This hypothesis is inconsistent with our results, as well as those of previous barometric and xenolith studies, which imply that rejuvenated-phase melts are generated within the asthenosphere and rise to the surface without significant modification within the lithosphere [Clague and Dalrymple 1987; Garcia et al. 2010; Borisova and Tilhac 2021]. Second, as the plume spreads out beneath the plate it may entrain and melt compositionally distinct background mantle [Hofmann and Farnetani 2013]. As discussed by Hofmann and Farnetani [2013], this mechanism would be accompanied by a pronounced decrease in T_p relative to preceding phases, which we do not observe. Third, the plume may include multiple lithologies, specifically a more enriched lithology in the plume interior relative to its margins. Possible additional components include: fusible material such as pyroxenite or carbon-rich peridotite in the conduit's interior [Ballmer et al. 2011; Garcia et al. 2016; Borisova and Tilhac 2021; or an isotopically depleted lithology on its exterior [Hofmann and Farnetani 2013]. The similarity in our T_p estimates for each phase, along with our greater estimated equilibration depths for enriched, rejuvenated-phase melts, is consistent with this third mechanism. Precisely how melting of distinct plume lithologies might lead to an eruptive hiatus and subsequent eruption of the rejuvenated phase remains unclear and will be an important topic for future research.

We note that the Plank and Forsyth [2016] thermobarometer, like all the thermobarometers implemented thus far in meltPT, relies on the presence of olivine and orthopyroxene [see e.g. Lee et al. 2009; Till et al. 2012]. These methods cannot be accurately applied to melts generated from, and equilibrated with olivine-free pyroxenites (though pyroxenite-derived melts that re-equilibrate with olivine-bearing peridotite during their ascent could be appropriate to use). Cor-

relations between our melt-equilibration results and trace-element ratios, such as Sm/Yb, suggest that the possible presence of pyroxenite in the mantle source has not significantly affected our results (Figure 5G–L). Nevertheless, melt-equilibration estimates using rocks from regions where pyroxenites are postulated must be treated with caution.

4.3.4 Loa and Kea trends

Since \sim 3 Ma, Hawaiian volcanism has been divided into two sub-parallel volcanic tracks known as the Loa and Kea trends (Figure 3A). These trends are distinguished on the basis of chemistry: the Loa trend is more isotopically enriched, has lower CaO, and higher SiO₂ than the Kea trend, amongst a number of other geochemical differences [e.g. Figure 6B,D; Weis et al. 2011; Jackson et al. 2012].

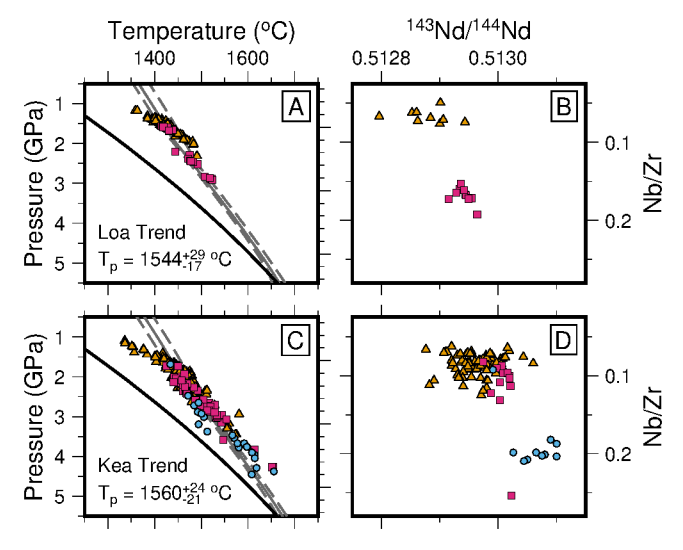


Figure 6: Comparison between Loa and Kea trends. [A] Temperature plotted as function of depth/pressure for Mauna Loa data. Figure set-up same as Figure 5. Mauna Loa trend includes data from Lāna'i, Kaho'olawe, the southwesterly Hawaiian volcanoes of Hualālai and Mauna Loa, as well as Penguin Bank. [B] ¹⁴³Nd/¹⁴⁴Nd ratios as function of Nb/Zr. [C]–[D] Same as panels [A] and [B] for Mauna Kea trend which includes data from Moloka'i, Maui and the northeasterly Hawaiian volcanoes (Kohala, Mauna Kea and Kīlauea).

Several theories have been proposed to explain the Loa and Kea geochemical trends, including the presence of two chemically distinct plumes, chemical heterogeneity within the plume, or the effects of spatially varying temperatures or lithospheric thicknesses [e.g. Bianco et al. 2005; Ballmer et al. 2011; Weis et al. 2011; Hofmann and Farnetani 2013; Dannberg and Gassmöller 2018]. Recently, Jones et al. [2017] proposed an alternative model linked to plume dynamics. Basal drag imparted by the lithosphere can influence plume-head spreading beneath the plate and bend the plume conduit in the direction of plate motion [Thoraval et al. 2006]. Jones et al. [2017] suggest that a well-documented change in plate motions at ~3 Ma initiated a slow realignment of the plume trail, during which the plume stem would no longer be aligned with plate motion, and the surface expressions of shallow and deep melting would be laterally offset. Loa-trend volcanoes may then sample shallow melting of an enriched pyroxenitic lithology that is not present beneath Kea-trend volcanoes.

A striking feature of the two trends is that rejuvenatedphase melts are only present in Kea-trend volcanoes (Figure 3B, Figure 6). In contrast, Loa-trend volcanoes exhibit only shield-phase melts that are some of the most isotopically depleted found in the Hawaiian islands (Figure 5S-X, Figure 6B,D). Our thermobarometric results suggest that rejuvenated-phase melts could be influenced by deep-melting of a isotopically enriched lithology, that may also be present to a lesser degree in shield-phase melts. We therefore propose a modification to the model of Jones et al. [2017], in which geochemical differences between the two trends are controlled by the presence or absence of a deep-melting, rather than shallow-melting, enriched lithology. In our conceptual model, prior to the establishment of distinct trends, shield-phase melts reflect a mixture of a less isotopically enriched, shallower melting lithology, and more enriched, deeper melting lithology. Over time, the deeper melting lithology becomes more important, culminating in the eruption of deep, isotopically enriched, rejuvenated-phase melts. As the plume conduit adjusts to the change in plate motions at ~3 Ma, Loa-trend volcanoes are isolated from the deep-melting, enriched lithology, so that their shield-phase melts are more isotopically depleted and the rejuvenated phase is completely absent. In contrast, Kea-trend volcanoes are influenced by the deep-melting, enriched lithology, so that their shield-phase melts are more isotopically enriched, and the rejuvenated phase is present (Figure 6B,D).

It is beyond our present scope to test this proposed model rigorously using, for example, convection simulations [e.g. Jones et al. 2017]. Nevertheless, we hope this example highlights the kinds of petrogenetic and geodynamic problems that major-element thermobaromtertric analyses can help to address.

5 Conclusions and future directions

In this study we present meltPT, an open-source Python package for estimating melt-equilibration conditions from mafic whole-rock data using a variety of thermobarometers, and for estimating melt fractions T_p by fitting adiabatic melt paths to melt-equilibration results [McNab and Ball 2023]. Here, we applied our software to two geologic regions: mid-ocean ridges and the Hawaiian Islands. meltPT is designed so that users will be able to easily add in new thermobarometers, additional methods for backtracking melt compositions, and other functionality; contributions are welcome via our public GitHub page (https://github.com/fmcnab/meltPT).

AUTHOR CONTRIBUTIONS

F. M. wrote the final version of meltPT and associated documentation. P. B. conducted the investigations of MORBs and the Hawaiian Islands. Both authors contributed equally to the conceptualisation of the model, first draft of meltPT, as well as the writing and editing of this manuscript.

ACKNOWLEDGEMENTS

F. M. was supported by ERC Consolidator Grant #863490 GyroSCoPe, awarded to T. Schildgen. P. B. acknowledges support by National Science Foundation Award number EAR-5329212. We are grateful to G. G. Roberts for providing us with a preliminary Python version of the Lee et al. [2009] thermobarometer. We are grateful to S. M. Brown Krein, C.-T. Lee, S. Matthews, C. Sun and C. B. Till for help implementing their respective methods.

DATA AVAILABILITY

All calculations were performed using meltPT v1.2.0. The compiled datasets used are available in the Supplementary Material alongside the online version of this article; scripts needed to reproduce the analyses are are available in the code repositories either via Zenodo (archived; https://doi.org/10.5281/zenodo.6948031) or GitHub (active development; https://github.com/fmcnab/meltPT). Full documentation with installation instructions and tutorials is available at http://meltpt.readthedocs.io. Tutorials can be run in a browser without the need for local installation via Binder (https://mybinder.org/v2/gh/fmcnab/meltPT/master).

COPYRIGHT NOTICE

© The Author(s) 2023. This article is distributed under the terms of the Creative Commons Attribution 4.0 International License, which permits unrestricted use, distribution, and reproduction in any medium, provided you give appropriate credit to the original author(s) and the source, provide a link to the Creative Commons license, and indicate if changes were made.

REFERENCES

- Abouchami, W., A. Hofmann, S. Galer, F. Frey, J. Eisele, and M. Feigenson (2005). "Lead isotopes reveal bilateral asymmetry and vertical continuity in the Hawaiian mantle plume". *Nature* 434(7035), pages 851–856. DOI: 10.1038/nature03402.
- Asimow, P. D. and C. H. Langmuir (2003). "The importance of water to oceanic mantle melting regimes". *Nature* 421(6925), pages 815–820. DOI: 10.1038/nature01429.
- Ball, P. W., T. Duvernay, and D. Davies (2022). "A Coupled Geochemical-Geodynamic Approach for Predicting Mantle Melting in Space and Time". *Geochemistry, Geophysics, Geosystems* 23(4), e2022GC010421. DOI: 10.1029/2022GC010421.
- Ball, P. W., N. J. White, J. Maclennan, and S. N. Stevenson (2021). "Global influence of mantle temperature and plate thickness on intraplate volcanism". *Nature Communications* 12(2045), pages 1–13. DOI: 10.1038/s41467-021-22323-9.
- Ball, P. W., N. J. White, A. Masoud, S. Nixon, M. Hoggard, J. Maclennan, F. Stuart, C. Oppenheimer, and S. Kröpelin (2019). "Quantifying asthenospheric and lithospheric controls on mafic magmatism across North Africa". Geochemistry, Geophysics, Geosystems 20, pages 3520–3555. DOI: 10.1029/2019GC008303.

- Ballmer, M. D., G. Ito, J. Van Hunen, and P. J. Tackley (2011). "Spatial and temporal variability in Hawaiian hotspot volcanism induced by small-scale convection". *Nature Geoscience* 4(7), pages 457–460. DOI: 10.1038/ngeo1187.
- Bao, X., C. R. Lithgow-Bertelloni, M. G. Jackson, and B. Romanowicz (2022). "On the relative temperatures of Earth's volcanic hotspots and mid-ocean ridges". *Science* 375(6576), pages 57–61. DOI: 10.1126/science.abj8944.
- Beattie, P. (1993). "Olivine-melt and orthopyroxene-melt equilibria". Contributions to Mineralogy and Petrology 115(1), pages 103–111. DOI: 10.1007/BF00712982.
- Bianco, T. A., G. Ito, J. M. Becker, and M. O. Garcia (2005). "Secondary Hawaiian volcanism formed by flexural arch decompression". *Geochemistry, Geophysics, Geosystems* 6(8). DOI: 10.1029/2005GC000945.
- Borisova, A. Y. and R. Tilhac (2021). "Derivation of Hawaiian rejuvenated magmas from deep carbonated mantle sources: A review of experimental and natural constraints". *Earth-Science Reviews* 222, page 103819. DOI: 10.1016/j.earscirev.2021.103819.
- Brounce, M. N., K. A. Kelley, and E. Cottrell (2014). "Variations in Fe³⁺/ Σ Fe of Mariana Arc basalts and mantle wedge fO_2 ". Journal of Petrology 55(12), pages 2513–2536. DOI: 10.1093/petrology/egu065.
- Brounce, M. N., E. Stolper, and J. Eiler (2017). "Redox variations in Mauna Kea lavas, the oxygen fugacity of the Hawaiian plume, and the role of volcanic gases in Earth's oxygenation". Proceedings of the National Academy of Sciences 114(34), pages 8997–9002. DOI: 10.1073/pnas.1619527114.
- Brown Krein, S., Z. Molitor, and T. Grove (2021). "ReversePetrogen: A Multiphase Dry Reverse Fractional Crystallization—Mantle Melting Thermobarometer Applied to 13,589 Mid-Ocean Ridge Basalt Glasses". Journal of Geophysical Research: Solid Earth 126(8), e2020JB021292. DOI: 10.1029/2020JB021292.
- Canil, D. (2002). "Vanadium in peridotites, mantle redox and tectonic environments: Archean to present". *Earth and Planetary Science Letters* 195(1-2), pages 75–90. DOI: 10.1016/S0012-821X(01)00582-9.
- Chen, C.-Y. and F. A. Frey (1985). "Trace element and isotopic geochemistry of lavas from Haleakala volcano, East Maui, Hawaii: implications for the origin of Hawaiian basalts". *Journal of Geophysical Research: Solid Earth* 90(B10), pages 8743–8768. DOI: 10.1029/JB090iB10p08743.
- Clague, D. A. and G. B. Dalrymple (1987). "The Hawaiian-Emperor volcanic chain, part 1, geologic evolution". *Volcanism in Hawaii*. Edited by R. W. Decker, T. L. Wright, and P. H. Stauffer. Hawaiian Volcano Observatory, pages 1–48. [U.S. Geological Survey Professional Paper 1350].
- Clague, D. A. and F. A. Frey (1982). "Petrology and trace element geochemistry of the Honolulu volcanics, Oahu: Implications for the oceanic mantle below Hawaii". *Journal of Petrology* 23(3), pages 447–504. ISSN: 00223530. DOI: 10.1093/petrology/23.3.447.
- Clague, D. A. and D. R. Sherrod (2014). "Growth and degradation of Hawaiian volcanoes". Characteristics of Hawaiian volcanoes 1801, pages 97–146. DOI: 10.3133/pp18013. [U.S. Geological Survey Professional Paper 1801].

- Condie, K. C., R. C. Aster, and J. Van Hunen (2016). "A great thermal divergence in the mantle beginning 2.5 Ga: Geochemical constraints from greenstone basalts and komatiites". *Geoscience Frontiers* 7(4), pages 543–553. DOI: 10.1016/j.gsf.2016.01.006.
- Courtier, A. M., M. G. Jackson, J. F. Lawrence, Z. Wang, C.-T. A. Lee, R. Halama, J. M. Warren, R. Workman, W. Xu, M. M. Hirschmann, et al. (2007). "Correlation of seismic and petrologic thermometers suggests deep thermal anomalies beneath hotspots". Earth and Planetary Science Letters 264(1-2), pages 308–316. DOI: 10.1016/j.epsl.2007.10.003.
- Cousens, B. L. and D. A. Clague (2015). "Shield to rejuvenated stage volcanism on Kauai and Niihau, Hawaiian Islands". Journal of Petrology 56(8), pages 1547–1584. DOI: 10.1093/petrology/egv045.
- Dalton, C. A., C. H. Langmuir, and A. Gale (2014). "Geophysical and geochemical evidence for deep temperature variations beneath mid-ocean ridges". *Science* 344(6179), pages 80–83. DOI: 10.1126/science.1249466.
- Dannberg, J. and R. Gassmöller (2018). "Chemical trends in ocean islands explained by plume–slab interaction". *Proceedings of the National Academy of Sciences* 115(17), pages 4351–4356. DOI: 10.1073/pnas.1714125115.
- Dasgupta, R., H. Chi, N. Shimizu, A. S. Buono, and D. Walker (2013). "Carbon solution and partitioning between metallic and silicate melts in a shallow magma ocean: Implications for the origin and distribution of terrestrial carbon". Geochimica et Cosmochimica Acta 102, pages 191–212. DOI: 10.1016/j.gca.2012.10.011.
- Dixon, J. E. and D. A. Clague (2001). "Volatiles in basaltic glasses from Loihi Seamount, Hawaii: Evidence for a relatively dry plume component". *Journal of Petrology* 42(3), pages 627–654. DOI: 10.1093/petrology/42.3.627.
- Dixon, J. E., D. A. Clague, B. Cousens, M. L. Monsalve, and J. Uhl (2008). "Carbonatite and silicate melt metasomatism of the mantle surrounding the Hawaiian plume: Evidence from volatiles, trace elements, and radiogenic isotopes in rejuvenated-stage lavas from Niihau, Hawaii". Geochemistry, Geophysics, Geosystems 9(9). ISSN: 15252027. DOI: 10.1029/2008GC002076.
- Dixon, J. E., D. A. Clague, P. Wallace, and R. Poreda (1997). "Volatiles in alkalic basalts form the North Arch Volcanic Field, Hawaii: extensive degassing of deep submarine-erupted alkalic series lavas". *Journal of Petrology* 38(7), pages 911–939. DOI: 10.1093/petroj/38.7.911.
- Forsyth, D. and S. Uyeda (1975). "On the relative importance of the driving forces of plate motion". *Geophysical Journal International* 43(1), pages 163–200. DOI: 10.1111/j.1365-246x.1975.tb00631.x.
- Frey, F. A. and J. M. Rhodes (1993). "Intershield geochemical differences among Hawaiian volcanoes: Implications for source compositions, melting process and magma ascent paths". *Philosophical Transactions of the Royal Society of London. Series A: Physical and Engineering Sciences* 342(1663), pages 121–136. DOI: 10.1098/rsta.1993.0009.
- Gale, A., C. A. Dalton, C. H. Langmuir, Y. Su, and J.-G. Schilling (2013). "The mean composition of ocean ridge

- basalts". Geochemistry, Geophysics, Geosystems 14(3), pages 489–518. DOI: 10.1002/ggge.20038.
- Gale, A., C. H. Langmuir, and C. A. Dalton (2014). "The global systematics of ocean ridge basalts and their origin". *Journal of Petrology* 55(6), pages 1051–1082. DOI: 10.1093/petrology/egu017.
- Garcia, M. O., K. Swanson, C. Lormand, and M. D. Norman (2022). "Petrology of Koko Rift basalts: Hawai'i's most recent and atypical rejuvenation stage eruptive sequence". Journal of Volcanology and Geothermal Research 424, page 107504. DOI: 10.1016/j.jvolgeores.2022.107504.
- Garcia, M. O., L. Swinnard, D. Weis, A. R. Greene, T. Gami, H. Sano, and C. E. Gandy (2010). "Petrology, geochemistry and geochronology of Kaua'i lavas over 4.5 Myr: Implications for the origin of rejuvenated volcanism and the evolution of the Hawaiian plume". *Journal of Petrology* 51(7), pages 1507—1540. ISSN: 00223530. DOI: 10.1093/petrology/egq027.
- Garcia, M. O., D. Weis, B. R. Jicha, G. Ito, and D. Hanano (2016). "Petrology and geochronology of lavas from Ka'ula Volcano: Implications for rejuvenated volcanism of the Hawaiian mantle plume". Geochimica et Cosmochimica Acta 185, pages 278–301. ISSN: 00167037. DOI: 10.1016/j.gca.2016.03.025.
- Garcia, M. O., D. Weis, L. Swinnard, G. Ito, and A. J. Pietruszka (2015). "Petrology and geochemistry of volcanic rocks from the South Kauái swell volcano, Hawaíi: Implications for the lithology and composition of the hawaiian mantle plume". *Journal of Petrology* 56(6), pages 1173–1197. ISSN: 14602415. DOI: 10.1093/petrology/egv033.
- Grove, T. L., E. S. Holbig, J. A. Barr, C. B. Till, and M. J. Krawczynski (2013). "Melts of garnet lherzolite: experiments, models and comparison to melts of pyroxenite and carbonated lherzolite". *Contributions to Mineralogy and Petrology* 166(3), pages 887–910. DOI: 10.1007/s00410-013-0899-9.
- Gurriet, P. (1987). "A thermal model for the origin of posterosional alkalic lava, Hawaii". Earth and Planetary Science Letters 82(1-2), pages 153–158. DOI: 10.1016/0012-821x(87)90115-4.
- Harrison, L. N., D. Weis, and M. O. Garcia (2020). "The multiple depleted mantle components in the Hawaiian-Emperor chain". *Chemical Geology* 532, page 119324. DOI: 10.1016/j.chemgeo.2019.119324.
- Helz, R., E. Cottrell, M. N. Brounce, and K. A. Kelley (2017). "Olivine-melt relationships and syneruptive redox variations in the 1959 eruption of Kīlauea Volcano as revealed by XANES". *Journal of Volcanology and Geothermal Research* 333, pages 1–14. DOI: 10.1016/j.jvolgeores. 2016.12.006.
- Herzberg, C. and P. Asimow (2015). "PRIMELT 3 MEGA. XLSM software for primary magma calculation: peridotite primary magma MgO contents from the liquidus to the solidus". *Geochemistry, Geophysics, Geosystems* 16(2), pages 563–578. DOI: 10.1002/2014GC005631.
- Hofmann, A. W. and C. G. Farnetani (2013). "Two views of Hawaiian plume structure". Geochemistry, Geophysics, Geosystems 14(12), pages 5308–5322. DOI: 10.1002/2013gc004942.

- Hoggard, M. J., K. Czarnota, F. D. Richards, D. L. Huston, A. L. Jaques, and S. Ghelichkhan (2020). "Global distribution of sediment-hosted metals controlled by craton edge stability". *Nature Geoscience* 13(7), pages 504–510. DOI: 10.31223/osf.io/2kjvc.
- Ito, G. and J. J. Mahoney (2005). "Flow and melting of a heterogeneous mantle: 1. Method and importance to the geochemistry of ocean island and mid-ocean ridge basalts". Earth and Planetary Science Letters 230(1-2), pages 29–46. DOI: 10.1016/j.epsl.2004.10.035.
- Jackson, M. G., D. Weis, and S. Huang (2012). "Major element variations in Hawaiian shield lavas: Source features and perspectives from global ocean island basalt (OIB) systematics". Geochemistry, Geophysics, Geosystems 13(9). DOI: 10.1029/2012gc004268.
- Jones, T., D. R. Davies, I. Campbell, G. Iaffaldano, G. Yaxley, S. C. Kramer, and C. R. Wilson (2017). "The concurrent emergence and causes of double volcanic hotspot tracks on the Pacific plate". *Nature* 545(7655), pages 472–476. DOI: 10.1038/nature22054.
- Katz, R. F., M. Spiegelmann, and C. H. Langmuir (2003). "A new parameterization of hydrous mantle melting". *Geochemistry, Geophysics, Geosystems* 4(9). DOI: 10.1029/2002GC000433.
- Kay, R. W. and P. W. Gast (1973). "The rare earth content and origin of alkali-rich basalts". *The Journal of Geology* 81(6), pages 653–682. DOI: 10.1086/627919.
- Kinzler, R. J. and T. L. Grove (1992). "Primary magmas of midocean ridge basalts 1. Experiments and methods". *Journal of Geophysical Research: Solid Earth* 97(B5), pages 6885—6906. DOI: 10.1029/91jb02840.
- Klöcking, M., N. J. White, J. Maclennan, D. McKenzie, and J. G. Fitton (2018). "Quantitative Relationships Between Basalt Geochemistry, Shear Wave Velocity, and Asthenospheric Temperature Beneath Western North America". *Geochemistry, Geophysics, Geosystems* 19(9), pages 3376–3404. ISSN: 15252027. DOI: 10.1029/2018GC007559.
- Kress, V. C. and I. S. Carmichael (1991). "The compressibility of silicate liquids containing Fe₂O₃ and the effect of composition, temperature, oxygen fugacity and pressure on their redox states". Contributions to Mineralogy and Petrology 108(1), pages 82–92. DOI: 10.1007/bf00307328.
- Langmuir, C. H., E. M. Klein, and T. Plank (1992). "Petrological systematics of mid-ocean ridge basalts: Constraints on melt generation beneath ocean ridges". *Mantle Flow and Melt Generation at Mid-Ocean Ridges* 71, pages 183–280. DOI: 10.1029/gm071p0183.
- Lee, C. T. A., P. Luffi, T. Plank, H. Dalton, and W. P. Leeman (2009). "Constraints on the depths and temperatures of basaltic magma generation on Earth and other terrestrial planets using new thermobarometers for mafic magmas". Earth and Planetary Science Letters 279(1-2), pages 20—33. DOI: 10.1016/j.epsl.2008.12.020.
- Marske, J. and E. Hauri (2019). Major- and trace-element compositions of 915 melt inclusions and host olivines from Hawaiian shield volcanoes. DOI: 10.1594/IEDA/111193.

- [Version 1.0] Interdisciplinary Earth Data Alliance (IEDA) [Dataset].
- Matthews, S., K. Wong, and M. L. M. Gleeson (2022a). *pyMelt* (v1.960). Zenodo https://zenodo.org/record/6013925.
- (2022b). "pyMelt: An extensible Python engine for mantle melting calculations". Volcanica 5(2), pages 469–475. DOI: 10.30909/vol.05.02.469475.
- Matthews, S., K. Wong, O. Shorttle, M. Edmonds, and J. Maclennan (2021). "Do olivine crystallization temperatures faithfully record mantle temperature variability?" *Geochemistry, Geophysics, Geosystems.* DOI: 10.1029/2020GC009157.
- McKenzie, D. and R. K. O'Nions (1991). "Partial melt distributions from inversion of rare-earth element concentrations". Journal of Petrology 32(5), pages 1021–1091. DOI: 10.1093/petrology/32.5.1021.
- M^cNab, F., P. W. Ball, M. J. Hoggard, and N. J. White (2018). "Neogene uplift and magmatism of Anatolia: Insights from drainage analysis and basaltic geochemistry". *Geochemistry, Geophysics, Geosystems* 19(1), pages 175–213. DOI: 10.1002/2017gc007251.
- M^cNab, F. and P. W. Ball (2023). *meltPT* (*v1.2.0*). Zenodo https://doi.org/10.5281/zenodo.6948031.
- Moore, L., E. Gazel, and R. Bodnar (2021). "The volatile budget of Hawaiian magmatism: Constraints from melt inclusions from Haleakala volcano, Hawaii". *Journal of Volcanology and Geothermal Research* 410, page 107144. DOI: 10.1016/j.jvolgeores.2020.107144.
- Moussallam, Y., M. Edmonds, B. Scaillet, N. Peters, E. Gennaro, I. Sides, and C. Oppenheimer (2016). "The impact of degassing on the oxidation state of basaltic magmas: a case study of Kīlauea volcano". Earth and Planetary Science Letters 450, pages 317–325. DOI: 10.1016/j.epsl.2016.06.031.
- Plank, T. and D. Forsyth (2016). "Thermal structure and melting conditions in the mantle beneath the Basin and Range province from seismology and petrology". *Geochemistry, Geophysics, Geosystems* 17, pages 1312–1338. DOI: 10.1002/2015GC006205.
- Putirka, K. D. (2008a). "Excess temperatures at ocean islands: Implications for mantle layering and convection". *Geology* 36(4), pages 283–286. DOI: 10.1130/g24615a.1.
- (2008b). "Thermometers and barometers for volcanic systems". Reviews in Mineralogy and Geochemistry 69(1), pages 61–120. DOI: 10.1515/9781501508486-004.
- Putirka, K. D., M. Perfit, F. J. Ryerson, and M. G. Jackson (2007). "Ambient and excess mantle temperatures, olivine thermometry, and active vs. passive upwelling". *Chemical Geology* 241, pages 177–206. DOI: 10.1016/j.chemgeo. 2007.01.014.
- Putirka, K. D., Y. Tao, K. Hari, M. R. Perfit, M. G. Jackson, and R. Arevalo Jr (2018). "The mantle source of thermal plumes: Trace and minor elements in olivine and major oxides of primitive liquids (and why the olivine compositions don't matter)". American Mineralogist: Journal of Earth and Planetary Materials 103(8), pages 1253–1270. DOI: 10.2138/am-2018-6192.

- Reid, M. R., W. K. Schleiffarth, M. A. Cosca, J. R. Delph, J. Blichert-Toft, and K. M. Cooper (2017). "Shallow melting of MORB-like mantle under hot continental lithosphere, Central Anatolia". *Geochemistry, Geophysics, Geosystems* 18, pages 1866–1888. DOI: 10.1002/2016GC006772.
- Roberts, G. G., N. White, M. J. Hoggard, P. W. Ball, and C. Meenan (2018). "A Neogene history of mantle convective support beneath Borneo". Earth and Planetary Science Letters 496, pages 142–158. DOI: 10.1016/j.epsl.2018.05.043.
- Ruscitto, D. M., P. J. Wallace, L. B. Cooper, and T. Plank (2012). "Global variations in H₂O/Ce: 2. Relationships to arc magma geochemistry and volatile fluxes". *Geochemistry, Geophysics, Geosystems* 13(3). DOI: 10.1029/2011gc003887.
- Sakyi, P. A., R. Tanaka, K. Kobayashi, and E. Nakamura (2012). "Inherited Pb isotopic records in olivine antecryst-hosted melt inclusions from Hawaiian lavas". *Geochimica et Cosmochimica Acta* 95, pages 169–195. DOI: 10.1016/j.gca. 2012.07.025.
- Sato, M. (1978). "Oxygen fugacity of basaltic magmas and the role of gas-forming elements". *Geophysical Research Letters* 5(6), pages 447–449. DOI: 10.1029/gl005i006p00447.
- Shimizu, N. and I. Kushiro (1975). "The partitioning of rare earth elements between garnet and liquid at high pressures: preliminary experiments". *Geophysical Research Letters* 2(10), pages 413–416. DOI: 10.1029/gl002i010p00413.
- Sides, I. R., M. Edmonds, J. Maclennan, D. A. Swanson, and B. F. Houghton (2014). "Eruption style at Kilauea Volcano in Hawai'i linked to primary melt composition". Nature Geoscience 7(6), pages 464–469. ISSN: 17520908. DOI: 10.1038/ngeo2140.
- Sinton, J. M., D. E. Eason, and R. A. Duncan (2017). "Volcanic evolution of Moloka'i, Hawai'i: Implications for the shield to postshield transition in Hawaiian volcanoes". Journal of Volcanology and Geothermal Research 340, pages 30–51. DOI: 10.1016/j.jvolgeores.2017.04.011.
- Stephenson, S. N., N. White, A. Carter, D. Seward, P. Ball, and M. Klöcking (2021). "Cenozoic dynamic topography of Madagascar". Geochemistry, Geophysics, Geosystems 22(6), e2020GC009624. DOI: 10.1029/2020gc009624.
- Sun, C. and R. Dasgupta (2020). "Thermobarometry of CO₂-rich, silica-undersaturated melts constrains cratonic lithosphere thinning through time in areas of kimberlitic magmatism". Earth and Planetary Science Letters 550, page 116549. DOI: 10.1016/j.epsl.2020.116549.
- Tamura, Y., M. Yuhara, and T. Ishii (2000). "Primary arc basalts from Daisen volcano, Japan: equilibrium crystal fractionation versus disequilibrium fractionation during su-

- percooling". Journal of Petrology 41(3), pages 431–448. DOI: 10.1093/petrology/41.3.431.
- Thoraval, C., A. Tommasi, and M.-P. Doin (2006). "Plume-lithosphere interaction beneath a fast moving plate". Geophysical Research Letters 33(1). DOI: 10.1029/2005gl024047.
- Till, C. B., T. L. Grove, and M. J. Krawczynski (2012). "A melting model for variably depleted and enriched lherzolite in the plagioclase and spinel stability fields". *Journal of Geophysical Research: Solid Earth* 117(B6). DOI: 10.1029/2011jb009044.
- Tucker, J. M., E. H. Hauri, A. J. Pietruszka, M. O. Garcia, J. P. Marske, and F. A. Trusdell (2019). "A high carbon content of the Hawaiian mantle from olivine-hosted melt inclusions". *Geochimica et Cosmochimica Acta* 254, pages 156–172. DOI: 10.1016/j.gca.2019.04.001.
- Weis, D., M. O. Garcia, J. M. Rhodes, M. Jellinek, and J. S. Scoates (2011). "Role of the deep mantle in generating the compositional asymmetry of the Hawaiian mantle plume". *Nature Geoscience* 4(12), pages 831–838. DOI: 10.1038/ngeo1328.
- Wieser, P. E., M. Petrelli, J. Lubbers, E. Wieser, S. Özaydın, A. J. R. Kent, and C. B. Till (2022). "thermombar: An open-source Python3 tool for thermobarometry and hygrometry". *Volcanica* 5(2), pages 349–384. DOI: 10.30909/vol.05.02.349384.
- Wieser, P. E., M. Edmonds, J. Maclennan, F. E. Jenner, and B. E. Kunz (2019). "Crystal scavenging from mush piles recorded by melt inclusions". *Nature Communications* 10(1), pages 1–11. DOI: 10.1038/s41467-019-13518-2.
- Wieser, P. E., H. Lamadrid, J. Maclennan, M. Edmonds, S. Matthews, K. Iacovino, F. E. Jenner, C. Gansecki, F. Trusdell, R. L. Lee, et al. (2021). "Reconstructing magma storage depths for the 2018 Kīlauean eruption from melt inclusion CO₂ contents: the importance of vapor bubbles". Geochemistry, Geophysics, Geosystems 22(2), e2020GC009364. DOI: 10.31223/x5x60v.
- Yang, A. Y., C. H. Langmuir, Y. Cai, P. Michael, S. L. Goldstein, and Z. Chen (2021). "A subduction influence on ocean ridge basalts outside the Pacific subduction shield". *Nature Communications* 12(1), pages 1–10. DOI: 10.1038/s41467-021-25027-2.
- Zhang, H. L., E. Cottrell, P. A. Solheid, K. A. Kelley, and M. M. Hirschmann (2018). "Determination of Fe³⁺/ΣFe of XANES basaltic glass standards by Mössbauer spectroscopy and its application to the oxidation state of iron in MORB". *Chemical Geology* 479, pages 166–175. DOI: 10.1016/j.chemgeo. 2018.01.006.